

1 Late Neogene terrestrial climate reconstruction of the Central
2 Namib Desert derived by the combination of U-Pb silcrete and
3 TCN exposure dating

4 Benedikt Ritter ^{1*}, Richard Albert ^{2,3*}, Aleksandr Rakipov ^{2,3}, Fredrik M. van der Wateren ⁴, Tibor
5 J. Dunai ¹, Axel Gerdes ^{2,3}

6
7 *1 Institute of Geology & Mineralogy, University of Cologne, Germany*

8 *2 Frankfurt Isotope and Element Research Center (FIERCE), Goethe-University Frankfurt, Germany*

9 *3 Institute of Geosciences, Goethe-University Frankfurt, Germany*

10 *4 Philosophical Practice, Cas Oorthuyskade 23, 1087 DP Amsterdam, Netherlands*

11 **Equal Contribution - Corresponding Authors*

12
13 *Corresponding authors:*

14 *Benedikt Ritter – benedikt.ritter@uni-koeln.de*

15 *Richard Albert - AlbertRoper@em.uni-frankfurt.de*

16 **Keywords:** Namib Desert, U-Pb dating, groundwater sil-/calcretes, cosmogenic nuclides

17 **Abstract:**

18 The chronology of the Cenozoic ‘Namib Group’ of the Namib Desert is rather poorly understood
19 and lacks direct radiometric dating. Thus, the paleoclimate and landscape evolution of the Central
20 Namib Desert remains imprecise, complicating the detailed search for global and/or local forcing
21 factors for the aridification of the Namib. The widespread occurrence of calcretes and silcretes in
22 the Namib Desert allows to apply the novel application of the U-Pb laser ablation dating technique
23 on sil- and calcretes, to date important phases of landscape stability and to retrieve critical
24 paleoclimatic and environmental information on desertification and its paleoclimatic variability.
25 Microscale silcrete formation (max. 8 mm) due to pressure solution by expanding calcrete
26 cementation provides the opportunity to date multiple phases (multiple generation of silcrete as
27 growing layers or shells) of silcrete formation. Groundwater sil- and calcrete formation occurred
28 at our study site during the Pliocene, a period of relatively stable climate and landscape conditions
29 under semi-arid to arid conditions. Terrestrial Cosmogenic Nuclide (TCN) exposure ages from flat
30 canyon rim surfaces indicate the cessation of groundwater calcrete formation due to incision
31 during the Late Pliocene/Early Pleistocene and mark a large-scale landscape rejuvenation due to

32 climate shifts towards more arid conditions in the Pleistocene, which can be connected to global
33 climate patterns. This study demonstrates the feasibility of applying U-Pb laser ablation to
34 groundwater sil- and calcretes, discusses several important issues associated with this technique
35 and opens up the possibility of dating numerous sedimentary sequences containing sil- and
36 calcretes in arid environments. In particular, the use of silcretes (as described above) reduces
37 potential effects of detrital components and bulk-signal measurements by using massive calcretes.
38 Our study redefines and improves the generally accepted Late Cenozoic chronostratigraphy of the
39 Namib Desert (Miller, 2008).

40 **1. Introduction**

41 In Namibia, widespread calcretes, together with (spatially) more restricted silcretes, are among
42 the most auspicious features of the Cenozoic surface cover and are outcropping along deeply
43 incised ephemeral or fossil drainage systems in terms of their ability to record past environmental
44 change (Miller, 2008; Candy et al., 2004; Summerfield, 1983a; Van Der Wateren and Dunai, 2001;
45 Ward, 1987). As well as being an important component in explaining the generally low denudation
46 rates due to their protective function (Stokes et al., 2007; Nash and Smith, 1998), these sil- and
47 calcretes are also thought to indicate relatively long periods of landscape and climate stability
48 during their formation (Goudie et al., 2015).

49 In general, calcretes are thought to form under semi-arid to arid conditions, with varying
50 interpretations and associations with specific precipitation ranges (Goudie, 2020; Summerfield,
51 1983a; Alonso-Zarza, 2003). Various models have been proposed to explain the different types of
52 calcrete (pedogenic, non-pedogenic, Goudie, 2020). In this study, we will mainly focus on the
53 non-pedogenic, groundwater-related calcrete formation, based on the *per-ascensum* hypothesis
54 (Goudie, 1996; Goudie et al., 2015), which are formed mainly by evaporation from the capillary
55 fringe or below the water table due to changing CO₂ level (Goudie et al., 2015). Most prominent
56 calcrete formations are related to calcretes capping the Karpfenkliff Conglomerate of the Kuiseb
57 Canyon in the Central Namib and the Kamberg Calcrete Formation (Fig. 1, Ward, 1987). Secondary
58 silcrete formation by pressure solution and reprecipitation was synchronous with calcrete
59 formation in the Karpfenkliff conglomerates. It consists of microscale silcrete with discrete
60 multiple layers of silcrete encrusting quartz clasts. The Karpfenkliff Conglomerate overlies the
61 Tsondab Sandstone and was probably deposited in a proto-Kuiseb and a proto-Gaub valley (Ward
62 et al., 1983; Miller, 2008; Ward, 1987).

63 Calcretes in the central Namib are thought to be at least Early Pleistocene to Pliocene in age (Ward,
64 1987; Miller, 2008). Common dating techniques used to date calcretes are radiocarbon ¹⁴C, U/Th
65 disequilibrium, or solution U-Pb. The first two dating methods are limited to ~45 kyr or 500 kyr,

66 respectively. Calcrete U-Pb laser ablation has recently been used to provide critical chronological
67 information on the age-depth relationship of the calcretized sediments from the Kalahari Group
68 (Houben et al., 2020). However, the dating of calcretes using the U-Pb system may be
69 influenced/biased by detrital components from the source area of the leached carbonates. The
70 variable growth rate makes it difficult to obtain individual ages from multiple generations of
71 calcrete formation when using the bulk sampling approach for solution U-Pb dating, as it can be
72 affected by the 'nugget' effect (Branca et al., 2005). Although calcrete formation pre-dates the
73 major canyon incision that can be dated using TCN exposure dating, calcrete formation post-dates
74 sediment deposition and is not age-equivalent to the host sediments. However, the time lag
75 between sediment deposition and calcrete formation may be negligible for any expected age in
76 the range of several millions of years. To avoid contamination by detrital components from the
77 catchment and to date multiple stages of sil-/calcrete formation, syndepositional (with calcrete
78 formation), microscale silcretes produced by the secondary effect of calcrete formation, pressure
79 solution and re-precipitation in the proximity (pressure shadow) might be a valuable target.

80 Evidence for climate change and major landscape change, as well as the reliability of dating of
81 Plio/Pleistocene sediments in the Namib, is relatively poor and not well constrained, and in part
82 shows discrepancies between different dating techniques and interpretations (Miller, 2008; Van
83 Der Wateren and Dunai, 2001; Goudie and Viles, 2014). In Namibia, calcretes and silcretes
84 commonly form prominent landscape features (i.e., cliffs) outcropping along deeply incised
85 ephemeral or fossil drainage systems (Miller, 2008; Van Der Wateren and Dunai, 2001; Ward,
86 1987). The (relative) chronology of these fossil duricrusts is the backbone of the (late) Cenozoic
87 chronostratigraphy of the Namib Desert ('Namib Group' of Miller, 2008) and past climate
88 reconstructions (Miller, 2008, and references therein). A major weakness of this
89 chronostratigraphy is its absolute chronology: essentially all early Quaternary to mid- Miocene
90 continental deposits in the Namib Desert are 'dated' with ostrich shells (Miller, 2008) or are
91 age-correlated with deposits dated with such shells (Miller, 2008). In general, the ostrich shell
92 biostratigraphy is linked to intracontinental correlations derived from fossil mammals (Pickford
93 and Senut, 2000). The catch is that only the oldest shells are 'dated' to 16-20 Ma (Aepyonithoid,
94 Senut, 2000; Pickford et al., 1999; Pickford et al., 1995), whereas the ensuing eight ostrich species
95 are arbitrarily assigned to 2 to 3 Myr long periods (Senut, 2000) without any direct age control.
96 The ostrich shell biostratigraphy provides a valuable relative chronology, but its use in its current
97 form as an absolute chronology remains unverified for the time < 16 Ma. Consequently, the
98 generally accepted Late Cenozoic chronostratigraphy of the Namib Desert (Miller, 2008) requires
99 verification.

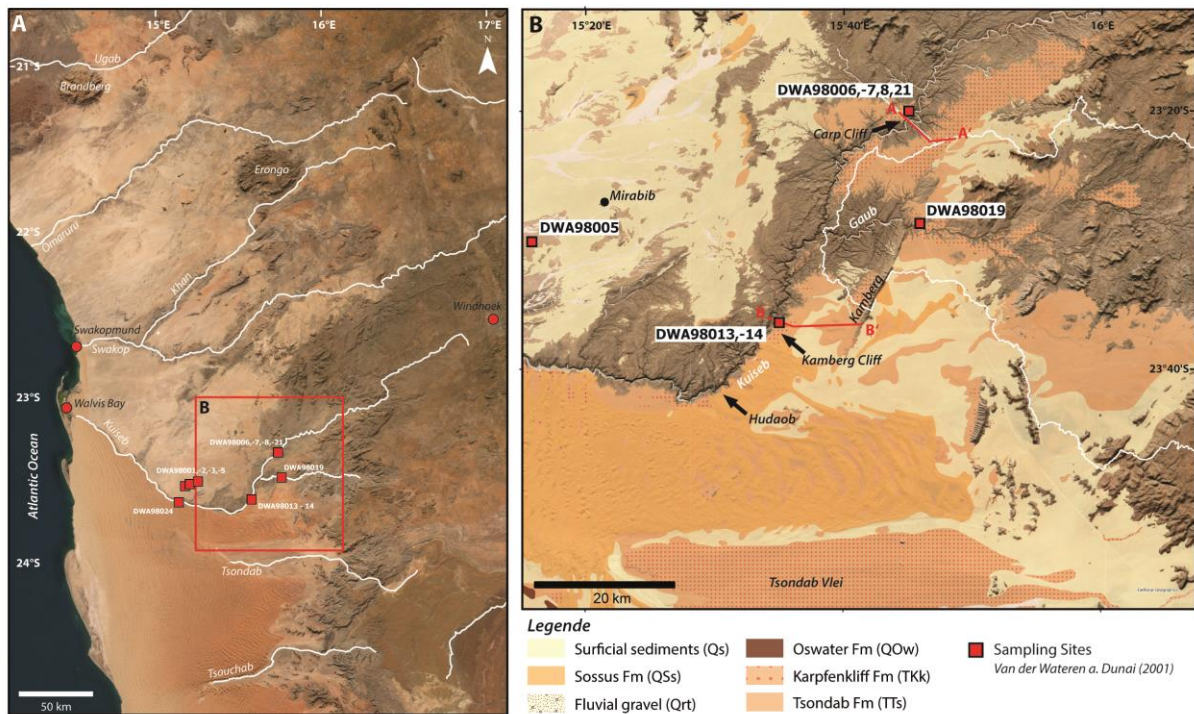
100 The use of Terrestrial Cosmogenic Nuclide (TCN) exposure dating in the Namib Desert has grown
101 in recent years, demonstrating that this method is a reliable way to measure landscape change

102 (Van Der Wateren and Dunai, 2001; Vermeesch et al., 2010; Stone, 2013; Bierman and Caffee,
103 2001). According to Van Der Wateren and Dunai (2001), major changes in the Namib Desert, i.e.
104 rejuvenation of the landscape by intermittent fluvial phases during the predominant arid to
105 hyperarid climate, indicate major changes during the Plio-/Pleistocene. However, there are
106 doubts about the interpretation of the exposure ages in relation to the underlying deposited
107 sediments (Miller, 2008). The dating of groundwater connected sil- and calcretes beneath the
108 surfaces sampled for TCN exposure dating allows to verify the resulting TCN exposure ages.
109 Furthermore, the combination of both dating techniques can be used to build a robust chronology
110 of landscape change during the evolution and intensification of arid conditions in the Namib
111 Desert.

112 Here we present the new application of U-Pb laser ablation to groundwater silcretes from the
113 Namib Desert in combination with re-measured TCN exposure ages from the Karpfenkliff and
114 nearby equivalent sites. Laser ablation U-Pb dating of multiple microscale silcrete layers from the
115 Karpfenkliff Conglomerate Formation indicates groundwater cal-/silcrete formation during the
116 Pliocene. Re-measured surface clasts from Van Der Wateren and Dunai (2001) confirm and
117 substantiate the interpretation of a major landscape rejuvenation of the Central Namib during the
118 Plio-/Pleistocene transition. The combination of the two dating techniques allows a robust
119 chronological reconstruction of landscape evolution and the paleoclimate transition to
120 increasingly arid conditions in the central Namib Desert.

121 **2. Sampling Site and Samples**

122 The central Namib Desert, between the Atlantic Ocean to the west and the Great Escarpment to
123 the east, is a relatively flat landscape with numerous dispersed inselbergs and locally deeply
124 incised canyons formed by ephemeral rivers such as the Kuiseb or Swakop (Fig. 1). Our study
125 focuses on the Kuiseb River canyon in the central Namib. The ephemeral Kuiseb River marks the
126 prominent boundary between the stone desert in the north and the Namib Sand Sea to the south.
127 The Kuiseb River receives its water from precipitation in the Great Escarpment to the east, with
128 mean annual rainfall of 200-450 mm/yr (Ward, 1987; Jacobson et al., 1995). Annual floods of the
129 Kuiseb River clean its bed of all sand transported from the Namib Sand Sea to the south. They only
130 reach the sea during exceptionally high floods (Van Der Wateren and Dunai, 2001). The Kuiseb
131 River forms a distinctive deep and partly narrow canyon, which is up to 250 m deep and only
132 1000 m wide at its deepest part (Fig. 1, 2). The recent course of the Kuiseb River is south-
133 southwest to Hudaob, where it is thought to have been redirected north-west by the activity of the
134 Namib Sand Sea (Miller, 2008). Prior to this deflection, the Proto-Kuiseb River may have flowed
135 westwards, as indicated by numerous outcrops within the interdune valleys of the Namib Sand
136 Sea (Fig. 25.18 Vol. 3 in Miller, 2008; Ward, 1987; Lancaster, 1984).



137

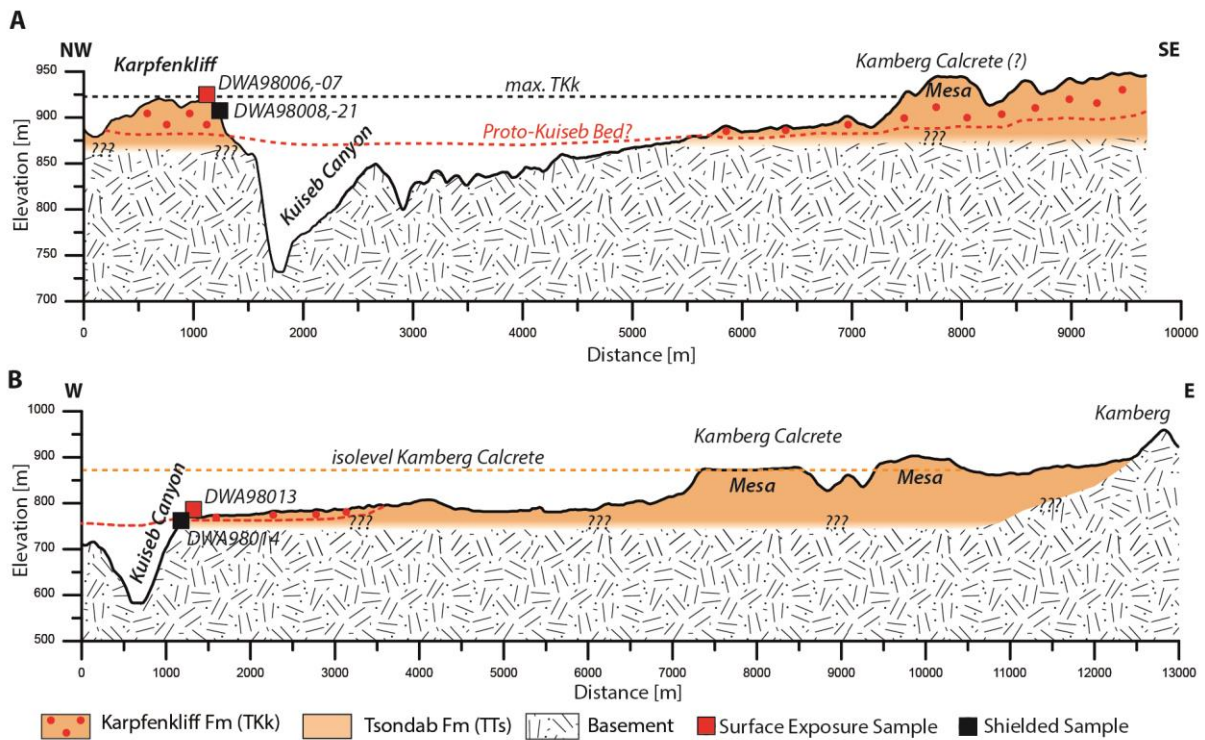
138 *Fig. 1: (A) Overview map of the Central Namib Desert based on World Imagery (Earthstar*
 139 *Geographics (TerraColor NextGen) imagery, ArcGIS Pro Version 3.1.0). Major drainage systems are*
 140 *shown in white. Red rectangle indicates the study area. Red squares indicate sampling sites of Van*
 141 *Der Wateren and Dunai (2001). Topographic profiles in Fig. 2 are marked as red lines. (B) Study area*
 142 *(Earthstar Geographics (TerraColor NextGen) imagery, ArcGIS Pro Version 3.1.0) including mapped*
 143 *geology by the Geological Survey of Namibia (Geological Survey of Namibia, 2016). Relevant*
 144 *geological formations are shown covering the Cenozoic sediment succession of the Central Namib*
 145 *(Namib Group). Red squares indicate sampling sites from Van Der Wateren and Dunai (2001). The*
 146 *sub-catchment of the Gaub River is shown in white.*

147 Sediment Succession Kuiseb Canyon

148 The outcrop sequence along the Kuiseb canyon in our study area comprises up to 100 m of
 149 sedimentary units (Fig. 2) resting on the Namib Unconformity Surface of Precambrian age (NUS,
 150 Ward, 1987; Miller, 2008), consisting of basal breccias from Precambrian basement, and solidified
 151 aeolian sands assigned to the Tsondab Sandstone Formation, overlain by calcretized
 152 coarse-grained conglomerates, called the Karpfenkliff Conglomerate Formation (Ward, 1987).
 153 Well-preserved terraces, resistant to weathering due to calcretization, are exposed at the rim of
 154 the canyon (Fig. 3).

155 The Tsondab Sandstone Formation rests on the Namib Unconformity Surface (NUS, Ward, 1987;
 156 Miller, 2008), and is the oldest and first terrestrial Cenozoic deposit in the Central Namib (Ward,
 157 1987; Miller, 2008), covering large areas of the Central Namib (Fig. 1, 2). The Tsondab Sandstone
 158 Formation consists predominantly of cemented aeolianites (Miller, 2008; Ward, 1987) and is
 159 regarded as the precursor of the recent Namib Sand Sea (Ollier, 1977). The Tsondab Sandstone
 160 Formation is thought to have been deposited under predominantly arid conditions (Ward, 1987),

161 between 20-16 Ma and 5 Ma based on the biostratigraphy of *Struthious* eggshells (Namoris
 162 Oshanai, *Struthio Karinagarabensis*, Ward and Corbett, 1990; Pickford et al., 1995; Senut, 2000).



163

164 *Fig. 2: (A) Cross-sections of the Karpfenkliff and (B) Kamberg Cliff based on SRTM data*
 165 *(created using ArcGIS Pro 3.1.0). Spatial information on geological units was extrapolated from*
 166 *mapped geology (Geological Survey of Namibia, 2016). Samples were collected from the surface of*
 167 *the Karpfenkliff (DWA980006,07) and from the subsurface at the canyon outcrop (DWA980008, -*
 168 *21). The identical sampling approach was used on the Kamberg Cliff, by sampling exposed quartz*
 169 *clasts (DWA98013) and shielded clasts (DWA98014). The shielded quartz clasts were used to*
 170 *investigate and date secondary micro-scale silcrete layers attached to quartz clasts. Due to the*
 171 *unknown fluvial topography of the Proto-Kuseb, the profile is just an approximation. The occurrence*
 172 *of the Karpfenkliff Conglomerate Formation (TKk) is used from the geological map, however, its*
 173 *outcrop condition in profile A in the eastern sector remains speculative. The exact transition from*
 174 *the underlying Tsondab Sandstone (TTs) to the Karpfenkliff Conglomerate Formation is unclear and*
 175 *is approximated. The elevation of the Kamberg Calcrete from its key position is marked in B and to*
 176 *illustrate the potential discrepancy between the two formations.*

177 Proto-Kuseb Incision and aggradation of the Karpfenkliff Conglomerate Formation

178 The Karpfenkliff Conglomerate Formation (TKk, Ward, 1987) overlies the Tsondab Sandstone
 179 Formation and was deposited in a proto-Kuseb and proto-Gaub River valley, a tributary of the
 180 Kuseb River (Fig. 1, 2). Pre-depositional incision of the Kuseb and Gaub rivers probably occurred
 181 during a wetter phase (Ward, 1987; Miller, 2008). The incision excavated a broad shallow valley
 182 and eroded the semi-consolidated Tsondab Sandstone without eroding the underlying
 183 Pre-Cambrian Damaran schists (Ward, 1987; Miller, 2008). The Karpfenkliff Conglomerate
 184 Formation consists of a medium- to fine-grained, sand-sized matrix of angular to subrounded

185 clasts (Fig. 3, Ward, 1987; Miller, 2008). Clasts are rounded to well-rounded with numerous
186 percussion marks (Ward, 1987; Van Der Wateren and Dunai, 2001). The Karpfenkliff
187 Conglomerate Formation thins to the west, indicating a depositional wedge (Miller, 2008). The
188 thickest accumulations are found at the foothills of the Great Escarpment (~ 60 m, Miller, 2008),
189 decreasing to ~ 40 m (Ward, 1987) in the upper Gaub Valley, 20-30 m at the Karpfenkliff, and
190 thinning to ~5 m at Gomkaeb (Ward, 1987; Miller, 2008). Deposition took place in a wide, shallow,
191 braided river system (Ward, 1987; Miller, 2008), presumably during an intermittent pluvial phase
192 despite prevailing arid conditions and synchronous with the deposition of the Tsondab aeolianites
193 (Ward, 1987). Equivalent gravels in the Tsondab, Tsauchab and Swakop rivers are assigned to the
194 Karpfenkliff Conglomerate Formation (Miller, 2008). The conglomerate is cemented by a massive
195 groundwater calcrete that has caused significant volume expansion (Miller, 2008). The source
196 area of the carbonate ions is thought to be the outcropping and eroding Precambrian Nama Group
197 in the headwaters of the Kuiseb River and is therefore authogenic in origin. Calcretization caused
198 secondary precipitation of microscale silcrete by pressure solution and local re-precipitation.

199 The Karpfenkliff Conglomerate Formation is age-correlated with the occurrence of *Diamantornis*
200 *corbetti* (fossil ostrich shell) in the Tsondab Aeolianites at Elim (Pickford and Senut, 2000; Miller,
201 2008), implying a younger age of *Diamantornis corbetti* than 14-15 Ma, equivalent to the age of
202 the Arries Drift Formation (Miller, 2008). Youngest deposition age (prior to 2.81 ± 0.11 Ma) was
203 proposed by Van Der Wateren and Dunai (2001) based on ^{21}Ne exposure dating of abandoned
204 surfaces of the Kuiseb River. The latter indicates the minimum depositional age for the last
205 remnants of any fluvial transport and deposition of the Karpfenkliff Conglomerate Formation.
206 Although this age is controversial according to Miller (2008, page 25-27) based on the ostrich shell
207 biostratigraphy, it clearly indicates the onset of incision by the recent Kuiseb River.

208 Calcrete within Karpfenkliff Formation and Tsondab Sandstone - Kamberg calcrete formation

209 The Kamberg Calcrete is described as a pedogenic calcrete up to 5 m in thickness (Miller, 2008;
210 Ward, 1987; Yaalon and Ward, 1982). According to Miller (2008), it cements the upper
211 Karpfenkliff Conglomerate Formation in places, as well as the Tsondab Sandstone, which covers a
212 large area east of Homeb in the Kuiseb River (Miller, 2008; Ward, 1987; Yaalon and Ward, 1982).
213 The Kamberg Calcrete, as well as equivalent calcretes in the study area, represent the surface
214 predating the recent canyon incision of the Kuiseb and Gaub rivers. They are used as an important
215 stratigraphic marker horizon in the Cenozoic 'Namib Group' (Miller, 2008; Ward, 1987). Whether
216 the Kamberg Calcrete is identical to the calcrete of the Karpfenkliff can be questioned (Fig. 2). The
217 pedogenic Kamberg Calcrete may be transitional to the groundwater calcrete found at the
218 Karpfenkliff and therefore be syndepositional. If the Kamberg Calcrete at the key site at Kamberg
219 correlates with the Kamberg Cliff and the Carp Cliff at Kuiseb canyon, this would imply that it is

220 stratigraphically equivalent to or younger than the groundwater calcrete cementing the
221 Karpfenkliff Conglomerate Formation (Fig. 2). A late Miocene age has been suggested for the
222 evolution of the Kamberg Calcrete (Yaalon and Ward, 1982; Ward, 1987). The calcrete is thought
223 to have been formed under semi-arid conditions during a relatively long period of landscape
224 stability (Goudie et al., 2015; Ward, 1987), with seasonal precipitation of potentially 350-450 mm
225 in the headwaters, decreasing drastically to the west (Ward, 1987).

226 A clear differentiation between the Kamberg Calcrete and any calcretes overlying and/or within
227 the Karpfenkliff Conglomerate Formation is difficult. The Kamberg Calcrete is not specifically
228 mapped in the published geological maps (Geological Survey of Namibia, 2016). For our study, we
229 focused on near-surface clasts with silcrete at the Karpfenkliff. The clear spatial and evolutionary
230 differentiation, as well as the connection between the two, should be the focus of future research
231 to use their occurrence as a marker horizon in the Central Namib.

232 Kuiseb Incision – Phase of landscape rejuvenation

233 The incision of the Kuiseb River (and other adjacent rivers such as the Swakop to the north) is
234 thought to have begun at the end of the Neogene, synchronous with other major river systems in
235 South Africa (Ward, 1987; King, 1951; Partridge and Maud, 1987; Korn and Martin, 1957). The
236 recent incision was able to cut deeply into the Karpfenkliff Conglomerate Formation, the Tsondab
237 Sandstone Formation and also into the Pre-Cambrian Damaran schists (Miller, 2008; Van Der
238 Wateren and Dunai, 2001; Ward, 1987), forming a V-shaped valley and the famous Kuiseb canyon
239 (Fig. 3). The transition from the aggradation of the Karpfenkliff Conglomerate Formation and the
240 formation of calcretes, to the degradation and incision of the recent Kuiseb, Gaub and Swakop
241 rivers is thought to be related to either a tectonic- (King, 1955; Ward, 1987; Korn and Martin,
242 1957) or climatic control (Van Der Wateren and Dunai, 2001; Richards and Richards, 1987;
243 Weissel and Seidl, 1998).

244 Detailed sampling sites and sampling

245 We consider that the calcrete at our sampling sites (Karpfenkliff, and Kamberg Cliff, Fig. 1, 2, 3)
246 was formed primarily by groundwater interaction, due to its direct location near the present-day
247 Kuiseb canyon. We used sampled and dated (in-situ ^{21}Ne) surface quartz clasts from Van Der
248 Wateren and Dunai (2001), from abandoned exposed surfaces and shielded clasts from several
249 metres below the surface. Details of the sampling procedure and sampling sites are given in Van
250 Der Wateren and Dunai (2001). For this study we concentrated on surface quartz clasts from the
251 Carp Cliff (DWA98006, -07, -08, -21) and the Kamberg Cliff (DWA98013, -14) for re-measurement
252 of cosmogenic ^{21}Ne concentrations (Table 1). Eight quartz clasts from the Carp Cliff with visible
253 silcrete cementation were prepared for U-Pb laser ablation (DWA98008, Table 1). The following

254 descriptions are taken from Van Der Wateren and Dunai (2001) and partly adapted for additional
255 samples.



256

257 *Fig. 3: Outcrop image compilation. (A) From Van Der Wateren and Dunai (2001) Kamberg Cliff, ~15 m of*
258 *Karpfenkliff Conglomerates overlying ~15 m of Tsondab Sandstones. (B) Carp Cliff (Field Campaign 2018,*
259 *Photo B. Ritter). (C) Close-up of the calcrete-cemented Karpfenkliff Conglomerate Formation (Photo B. Ritter).*
260 *Rounded quartz clasts float in a matrix-supported fabric which is cemented by calcrete. Some clasts are*
261 *fractured by volume expansion of the calcrete, resulting in pressure solution and formation of micro-scale*
262 *silcrete. (D) Surface of the calcrete cemented Karpfenkliff (Photo B. Ritter).*

263 Carp Cliff (Kuisseb highest terrace)

264 DWA98006-07 (Site 6) is located on the horizontal upper surface of a mesa-shaped terrace
265 remnant 500 m west of the 200 m deep Kuisseb Canyon (Fig. 1, 2). The terrace has a surface area
266 of ~5 km² and is surrounded by steep, locally vertical and overhanging cliffs, which to the east and
267 south are nearly 50 m in height. The terrace surface consists of a desert pavement of mainly quartz
268 pebbles overlying up to 15 cm of sandy silt. This is underlain by 10–25 m of calcretized pebble
269 and boulder conglomerates of the Karpfenkliff Conglomerate Formation (Fig. 3). Van Der Wateren
270 and Dunai (2001) collected 40 rounded (DWA98007) and (sub-)angular pebbles (DWA98006)
271 with diameters between 2 and 6 cm. The site is located at the top of the mesa and is almost
272 horizontal, so that post depositional transport of the sampled pebbles by the Kuisseb River or local
273 precipitation can be excluded.

274 DWA98008 and DWA980021 (Site 7 and 19) are located next to small gullies running from the
 275 north side of the Carp Cliff mesa. At these sites, Van Der Wateren and Dunai (2001) collected
 276 shielded samples 5 m below the terrace surface. Van Der Wateren and Dunai (2001) sampled
 277 rounded pebbles from the ceilings of overhangs to ensure that the measured ^{21}Ne concentrations
 278 were derived only during hillslope and fluvial transport to their present site and not from
 279 subsequent exposure at the sampling site.

280 Kamberg Cliff (Kuseb highest terrace)

281 DWA98013 and DWA98014 are from a terrace on the Karpfenkliff Conglomerate Formation
 282 immediately adjacent to the nearly 250 m deep Kuseb Canyon, 30 km downstream of Carp Cliff
 283 (Fig. 1, 2, 3). The terrace surface is very similar to that of Carp Cliff, with a desert pavement of
 284 pebbles and cobbles on a sandy silt overlying 25 m of calcretized conglomerates. The Karpfenkliff
 285 Conglomerates rest on 30–50 m of the Tsondab Sandstone Formation, which forms the bulk of the
 286 cliff adjacent to the canyon. DWA98013 sampling site is on the horizontal surface of the terrace,
 287 where we sampled angular pebbles. At DWA98014, rounded pebbles (DWA98014) were sampled
 288 from the ceiling of an overhang in the cliff face 6 m below.

289 Table 1: General sample information.

TCN Exposure Dating

Sample ID	Locality	Type	Longitude [°]	Latitude [°]	Remark
DWA98006Etch2	Carp Cliff	Quartz clasts	-23.339	15.744	amalgamated sample of 40 clasts
DWA98007Etch	Carp Cliff	Quartz clasts	-23.339	15.744	amalgamated sample of 40 clasts
DWA98008Etch2	Carp Cliff	Quartz clasts	-23.331	15.746	amalgamated sample of 40 clasts
DWA98021Etch	Carp Cliff	Quartz clasts	-23.332	15.745	amalgamated sample of 40 clasts
DWA98013Etch2	Kamberg Cliff	Quartz clasts	-23.608	15.580	amalgamated sample of 40 clasts
DWA98014Etch	Kamberg Cliff	Quartz clasts	-23.608	15.580	amalgamated sample of 40 clasts

U-Pb LA-ICP-MS Dating

Sample ID	Locality	Type	Longitude	Latitude	Remark
DWA98008- Silc3	Carp Cliff	Silcrete on clast	-23.331	15.746	Silcrete with distinct layering
DWA98008- Silc4	Carp Cliff	Silcrete on clast	-23.331	15.746	Silcrete with distinct layering
DWA98008- Silc7	Carp Cliff	Silcrete on clast	-23.331	15.746	Silcrete with distinct layering
DWA98008- Silc8	Carp Cliff	Silcrete on clast	-23.331	15.746	Silcrete with distinct layering

290

291

292

3. Formation of Calcretes and microscale silcretes

293
294 In general, two types of calcretes can be differentiated, pedogenic and groundwater calcretes
295 (Alonso-Zarza and Wright, 2010), following the *per descensum* or the *per ascensum* evolutionary
296 model (Goudie, 2020). They occur preferentially in arid to semi-arid climates (Alonso-Zarza,
297 2003; Candy and Black, 2009; Goudie, 2020). Specific climatic and environmental conditions are
298 required for calcrete formation; (1) precipitation in the headwater/source area to promote
299 carbonate dissolution, (2) intermittent or seasonal precipitation downstream favour
300 groundwater systems capable of (3) causing high evaporation and evapotranspiration for
301 chemical precipitation of carbonate (Mann and Horwitz, 1979). Calcrete formation is dependent
302 on the supply of carbonate ions leached from the drainage bedrock. In this study we focus on
303 groundwater calcretes formed along the Kuiseb- and Gaub rivers. Groundwater calcretes form at
304 or above shallow groundwater tables/aquifers (Mann and Horwitz, 1979; Netterberg, 1969) and
305 do not require subaerial exposure, although shallow contacts and stable surfaces favour the
306 evolution of groundwater calcretes (Alonso-Zarza, 2003). They were originally called 'valley
307 calcretes' (Butt et al., 1977) because of their relationship with drainages. Groundwater calcretes
308 are rather restricted to local drainages, although groundwater calcretes can have lateral extents
309 of more than 100 km long and 10 km wide, depending on the drainage topography (Mann and
310 Horwitz, 1979). Groundwater calcretes do not have characteristic features compared to
311 pedogenic calcretes and are rather massive bodies (Alonso-Zarza, 2003). The permeability
312 (coarse channel sediments) of the host rock favours their formation (Alonso-Zarza and Wright,
313 2010). Calcretes have been frequently used to obtain paleo precipitation information, but the
314 specific ranges are still under discussion. The upper limit may be between 600 and 1000 mm/yr
315 (Mack and James, 1994). The lower limit may be as low as 50 mm/yr (Goudie, 1973; Retallack,
316 1994).

317 Silcretes can form as duricrust due to the accumulation of secondary silica within a soil or host
318 rock (Milnes and Thiry, 1992; Summerfield, 1983a). Prominent examples include silcretes from
319 Australia (Milnes et al., 1991; Taylor and Eggleton, 2017) or the Kalahari Desert (Summerfield,
320 1983b; Nash and Shaw, 1998). In this study, we focus on microscale silcretes, which are formed
321 by pressure solution (Mcbride, 1989; Rutter, 1983; Sorby, 1863; Wilson, 2020) due to calcrete
322 cementation and volume expansion within the host rock or sediment, and therefore cannot be
323 directly compared to the commonly used term 'silcrete'. Additional silica may be enriched in the
324 groundwater due to increased pH (favours the precipitation of calcite and the solution of silica,
325 Goudie, 1983; Nash and Shaw, 1998). Microscale silcrete formation is therefore thought to be
326 linked to paleo-environmental and climatic conditions favourable to calcrete formation.
327 Calcretization involves the precipitation of CaCO_3 within the pore spaces of the host rock or
328 sediment, causing significant volume expansion. A secondary effect of this process is to increase

329 the differential pressure within the host rock or sediment, causing clast shattering, relocation and
330 pressure solution at intergranular contacts (Sorby, 1863; Rutter, 1983). Increased stress at grain
331 boundaries and intergranular contacts leads to dissolution, e.g., silica mobilisation. Mobilized
332 solutions migrate to regions of lower compressive stress, the 'pressure shadow', to reprecipitate.
333 Theoretically, depending on the remaining pore space, multiple pressure solution and
334 reprecipitation cycles can be archived in the host rock as multiple silcrete layers or shells attached
335 to quartz clasts.

336 **4. Dating of Cal- and Silcretes**

337 Quantifying the timing and duration of calcrete formation is quite difficult. Clear stratigraphic
338 relationships with the overlying and underlying sediments are not straightforward, as
339 groundwater calcrete, for example, forms within sediments deposited close to the surface.
340 Numerous studies propose only relative age controls and estimates of the formation time, such as
341 the application of the ostrich shell biochronostratigraphy used for the Namib Group (Pickford and
342 Senut, 2000; Senut, 2000; Miller, 2008). Many attempts have been made to date this type of
343 deposits using radiocarbon ^{14}C (e.g. Geyh and Eitel, 1997), U/Th (Kelly et al., 2000; Candy et al.,
344 2004; Candy and Black, 2009) or U-Pb dating (Rasbury and Cole, 2009; Houben et al., 2020).

345 Silcretes are enriched in U relative to calcretes and occur in most soils in arid and semi-arid
346 environments. Uranium decays to Pb isotopes through a chain of intermediate daughter isotopes,
347 and ages of thousands- to millions-of-years-old samples can be estimated using parent-daughter
348 pairs ^{238}U - ^{206}Pb , ^{235}U - ^{207}Pb , ^{234}U - ^{230}Th , and ^{238}U - ^{234}U . The use of a particular isotope pair depends
349 on how old the sample is compared to the half-life of the selected radioactive isotope within the U
350 decay chain (Neymark, 2011; Neymark et al., 2002, 2000). Considering that the samples are 2.85
351 Ma old or older (Van Der Wateren and Dunai, 2001), the U-Pb method using the parent-daughter
352 pairs ^{238}U - ^{206}Pb and ^{235}U - ^{207}Pb was chosen to date the samples in this work.

353 Many studies attempting to date massive cal-/silcretes are hampered by the dilution or averaging
354 effect of bulk analysis and by bias from non-carbonate detrital minerals or secondary
355 reprecipitated carbonate due to diagenesis. The "limestone dilution effect" (as a result of
356 contamination with detrital carbonate components of the host rock, Alonso-Zarza, 2003) or the
357 "averaging effect" (averaging of different phases of mineral precipitation, Candy and Black, 2009;
358 Neymark et al., 2000) are minimised (or even avoided) by the higher spatial resolution of laser
359 ablation compared to bulk analysis techniques. The possible effect of detrital components (e.g.
360 Zircon or clay minerals) on the U-Pb analyses is also neglected, as the signals from these inclusions
361 can be filtered out of the time-resolved analyses.

362 The conventional method of calculating U–Pb isotope dates assumes that all intermediate
363 daughter isotopes in the ^{238}U and ^{235}U decay chains were in secular equilibrium at the time of
364 formation (Neymark, 2014). This is not necessarily true for calcretes and silcretes due to
365 differences in the geochemical behaviour of parent and daughter elements. The silcretes dated in
366 this study are sufficiently old ($> c. 2.85 \text{ Ma}$) to have achieved secular equilibrium (at present), and
367 therefore (almost) all its initial excess of daughter isotopes to decay, or their initial depletion to
368 replenish (i.e. their activity ratios to be equal to 1) ergo a direct measurement of these deviations
369 is not feasible. Therefore, the values needed to correct for these disequilibriums were estimated
370 from previous works (see methodology chapter).

371

372 **5. Methods**

373 Raman Spectroscopy

374 We use Raman spectroscopy to obtain high resolution images of silcretes and to better
375 characterise the mineralogical composition. Raman spectra were collected with up to 1300
376 wavenumber (cm^{-1}), using a WITec alpha 300R confocal Micro-Raman microscope, at the Goethe
377 University Frankfurt (GUF). The objective used was 50x, an excitation laser of 532 nm (using 10
378 mW laser power before the objective), and spectra integration time of 0.2 s with 5 accumulations
379 in total. Maps ($400 \times 400 \mu\text{m}^2$) were performed applying a step size of $1.3 \mu\text{m}$ with a holographic
380 grating of $600 \text{ grooves mm}^{-1}$. The instrument was calibrated using an Ar-Hg spectral lamp and was
381 checked regarding its performance before the measurements with respect to the 1300 cm^{-1} line
382 of silicon. The spectrum of each sample layer was confirmed at several locations on the same layer.
383 Raman spectra of reference compounds are found in the Ruff database (<https://ruff.info/>).

384 Dating of Silcretes – U-Pb Laser Ablation ICP-MS

385 Eight quartz clasts were cut in half to expose their silcrete coatings, mounted in epoxy mounts and
386 polished at the Department of Geosciences, University of Cologne (UoC). U-Pb analyses were
387 performed at the Goethe University Frankfurt (GUF) using a RESolution 193 nm ArF excimer laser
388 (COMpex Pro 102), equipped with a two-volume ablation cell (Laurin Technic S155). The laser
389 was coupled to a ThermoScientific ElementXr sector field ICP-MS. The surfaces were cleaned with
390 8 pre-ablation laser pulses. Ablation was carried out in a He (0.3 l/min), Ar (1.01 l/min) and N
391 (0.012 l/min) atmosphere, with a high energy density ($c. 5 \text{ J/cm}^2$), a frequency of 15 Hz and round
392 $50 \mu\text{m}$ diameter spots (SI2_Supporting Information).

393 Artificial silicate glasses NIST SRTM 612 and 614 were used as reference materials (RM). Plots
394 and dates are calculated using the in- house spreadsheet program (Gerdes and Zeh, 2009, 2006),

395 together with Isoplot (Ludwig, 2012). Ages are reported with and without systematic components
396 (i.e., $\text{date} \pm 2s / 2s_{\text{sys}}$). Uncertainties include internal standard errors (SE), background, counting
397 statistics, excess scatter of the primary reference material (NIST SRTM 612), and excess variance
398 (calculated from NIST SRTM 614). Systematic uncertainties also propagate systematic errors,
399 which are the long-term excess variance (1.5%, 2s), decay constant uncertainties (Horstwood et
400 al., 2016) and the uncertainty derived from the initial activity ratio uncertainty. Dates are
401 calculated as Tera-Wasserburg lower intercepts (Tera and Wasserburg, 1972). Linear regressions
402 are anchored to a common-lead $^{207}\text{Pb}/^{206}\text{Pb}$ ratio of 0.837. This is the Y-intercept of sample
403 “DWA98008-Silc4 Black Crack”, which is where this ratio is better constrained. This value is in
404 good agreement with modelled crustal values at the time of formation (0.836, Stacey and Kramers,
405 1975).

406 The samples dated are sufficiently old to have reached secular equilibrium and hence activity
407 ratios cannot be measured (with the present techniques and assuming a closed system
408 behaviour). Consequently, the following initial activity ratios used are assumed. The silcretes
409 dated in this study have virtually no Th (average of ~ 89 ng/g) and therefore we consider
410 $[\text{^{230}Th}/\text{^{238}U}]_i = 0$ (initial $^{230}\text{Th}/^{238}\text{U}$ activity ratio). Considering previous studies on calcretes and
411 silcretes formed in semi-arid and arid environments (Oster et al., 2017; Maher et al., 2007;
412 Neymark, 2011), the ground and surface waters from which these rocks are formed often have
413 $[\text{^{234}U}/\text{^{238}U}]_i$ values greater than 1. Therefore, the data in this study are calculated with $[\text{^{234}U}/\text{^{238}U}]_i$
414 $= 1.75 \pm 0.32$ (2s abs), which is a weighted average of the $[\text{^{234}U}/\text{^{238}U}]_i$ of the above-mentioned
415 studies. The uncertainty in this activity ratio is added to the final systematic uncertainties by
416 quadratic propagation (Scardia et al., 2019; SI2_Supporting Information).

417 Cosmogenic ^{21}Ne Exposure Dating

418 We used prepared samples from Van Der Wateren and Dunai (2001) for in situ ^{21}Ne exposure
419 dating using the new noble gas mass spectrometer at the University of Cologne (Helix MC Plus
420 from Thermo Fisher Scientific, further information see Ritter et al., 2021). The ^{21}Ne analyses of
421 Van Der Wateren and Dunai (2001) were performed without an international standard (CREU).
422 For neon analysis we prepared amalgamated samples from each site containing between 35 and
423 40 quartz clasts (100mg/sample) using the already prepared 63-125 μm fraction. By also
424 analysing shielded pebbles, a pre-exposure correction (accumulated ^{21}Ne concentration during
425 transport) can be applied to analysed surface samples (Repka et al., 1997). The presumably
426 non-atmospheric ^{21}Ne concentration found in these samples can be subtracted from the
427 concentration in their exposed counterparts. The latter also corrects for any potential nucleogenic
428 ^{21}Ne that may be present in the samples. Samples were measured on the noble gas mass
429 spectrometer at the University of Cologne using the analytical methods outlined in Ritter et al.

430 (2021). CREU quartz standards were measured in Cologne for interlaboratory comparability and
 431 quality control (Vermeesch et al., 2015). The spallogenic origin of the measured ^{21}Ne excess was
 432 verified using the triple isotope plot. ^{21}Ne exposure ages were calculated using the ‘nuclide
 433 dependent scaling’ after Lifton et al. (2014), calculated with "The online exposure age calculator
 434 formerly known as the CRONUS-Earth online exposure age calculator." (Version 3,
 435 http://hess.ess.washington.edu/math/v3/v3_age_in.html; Balco et al., 2008).

436 6. Results

437 Silcrete Imaging

438 Digital microscope images show vein-contact parallel-layering with different crystal orientation
 439 (Fig. 4A and Supporting Information). The Raman spectra peaks at 129, 209 and 467 cm^{-1} are
 440 indicative for quartz, which dominate the silcrete samples. Raman spectroscopy of DWA98008-
 441 Silc8 also indicate the presence of one major calcite band (dark colour in Fig. 5B, Raman spectra
 442 peaks at 156, 283, 466, 714 and 1088 cm^{-1}). The calcite crack filling might be indicative for
 443 shattering of previous silcrete and crack filling by repeated and/or ongoing calcrete formation
 444 within the Karpfenkliff Conglomerate.

445 U-Pb Laser Ablation Results Silcretes

446 Four out of the eight silcrete samples yielded meaningful dates (DWA98008 – Silc3, Silc4, Silc7,
 447 Silc8), out of which 12 dates could be calculated from various silcrete layers (SI2_Supporting
 448 Information). The dates range from 2.96 ± 0.14 to 6.72 ± 0.16 Ma, with maximum relative
 449 abundance peaks at around 3.4 Ma and about 5.5 Ma (see Fig. 6 and Table 2). All dates are
 450 calculated from multiple spot analyses, ranging from 9 to 28 spots per date. The majority of the
 451 analyses have U concentrations between ~ 30 and $70 \mu\text{g/g}$, with an average of $42 \mu\text{g/g}$, and very
 452 low Th concentrations, up to 200ng/g , with an average of 89ng/g .

Sample name	Date (Ma) (1)	2s abs (2)	2s sys (3)	Y-Intercept (4)	2s (5)	Anchored (6)	MSWD (7)	n (8) (used)	n (9) (total)	Date (Ma) (10)	2s abs (11)	2s sys (12)
Silc3 Rim 1	5.756	0.124	0.132	0.837	0.008	WAHR	0.45	9	9	5.590	0.120	0.176
Silc3 Rim 2	5.246	0.107	0.115	0.837	0.008	WAHR	0.41	9	9	5.080	0.103	0.164
Silc3 Rim 3	5.488	0.068	0.081	0.837	0.008	WAHR	1.35	24	28	5.322	0.066	0.143
Silc3 Rim Outer	3.734	0.064	0.071	0.838	0.011	WAHR	1.63	28	28	3.569	0.061	0.138
Silc4 Black crack	5.927	0.244	0.248	0.8374	0.0066	FALSCH	1.50	21	25	5.761	0.237	0.270
Silc4 Rim	3.498	0.061	0.067	0.837	0.008	WAHR	1.24	16	17	3.332	0.058	0.136
Silc4 Rim Outer	3.456	0.061	0.067	0.837	0.008	WAHR	1.30	15	17	3.290	0.058	0.136
Silc4 Rim Inner	3.129	0.068	0.072	0.837	0.008	WAHR	1.63	9	9	2.964	0.064	0.138
Silc7	6.881	0.091	0.106	0.8528	0.0028	FALSCH	0.94	27	29	6.715	0.089	0.159
Silc8 Rim Out 1	6.116	0.081	0.095	0.837	0.008	WAHR	0.64	20	20	5.950	0.079	0.152
Silc8 Rim Out 2	5.131	0.132	0.139	0.837	0.014	WAHR	2.56	17	25	4.965	0.128	0.180

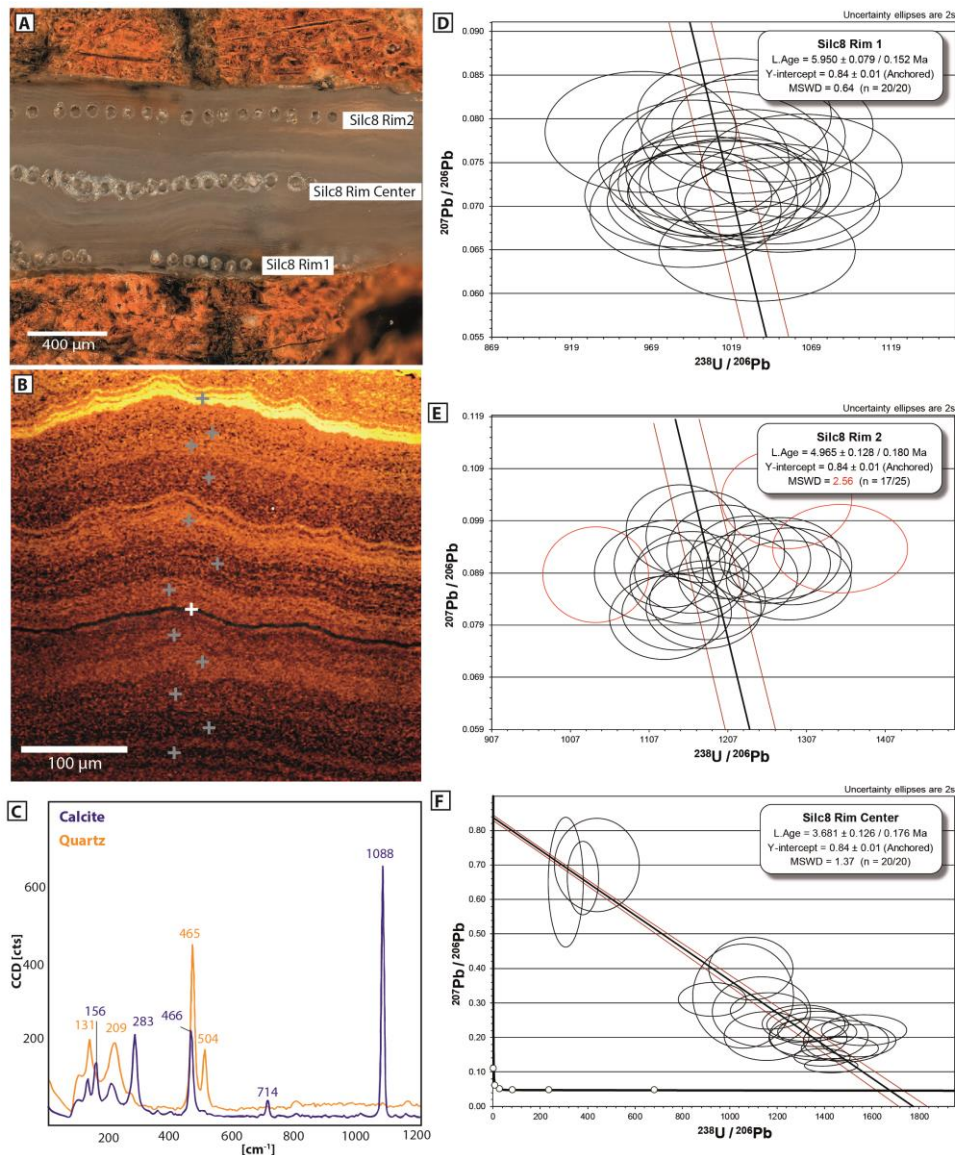
Silc8 Rim Center	3.847	0.131	0.135	0.837	0.008	WAHR	1.37	20	20	3.681	0.126	0.176
------------------	-------	-------	-------	-------	-------	------	------	----	----	-------	-------	-------

453

454 *Table 2: 1. - Concordia curve lower intercept dates, Tera-Wasserburg diagram (Tera and*
 455 *Wasserburg, 1972). 2. - 2s absolute uncertainties, considering within run precision (SE of the mean*
 456 *of ratios), excess of scatter, background, counting statistics and excess of variance (calculated from*
 457 *the validating RM, SRTM NIST 614. 2.6%, 1s, on $^{238}\text{U}/^{206}\text{Pb}$ and 0%, 1s, on $^{207}\text{Pb}/^{206}\text{Pb}$ ratios). 3. -*
 458 *Previous uncertainties (2) expanded with systematic uncertainties (0.8 %, 2s, long term*
 459 *reproducibility and decay constant uncertainties). See Horstwood et al. (2016). 4. - $^{207}\text{Pb}/^{206}\text{Pb}$ ratio*
 460 *of the upper intercept. 5. - 2s absolute uncertainty of the upper intercept. 6. - If the linear regression*
 461 *on the Tera-Wasserburg was anchored or not. 7. - Mean squared weighted deviates. 8. - Number of*
 462 *analyses considered. 9. - Total number of analyses. 10. - Dates calculated (following Wendt and Carl,*
 463 *1985) taking into account an initial $^{234}\text{U}/^{238}\text{U}$ activity ratio of 1.75, and initial $^{230}\text{Th}/^{238}\text{U}$ activity*
 464 *ratios of 0. 11. - Uncertainties (2) recalculated to the new dates (10). 12. - Uncertainties (3)*
 465 *recalculated to the new dates (10) and adding $^{234}\text{U}/^{238}\text{U}$ activity ratio uncertainty (0.32, 2s abs).*

466

467



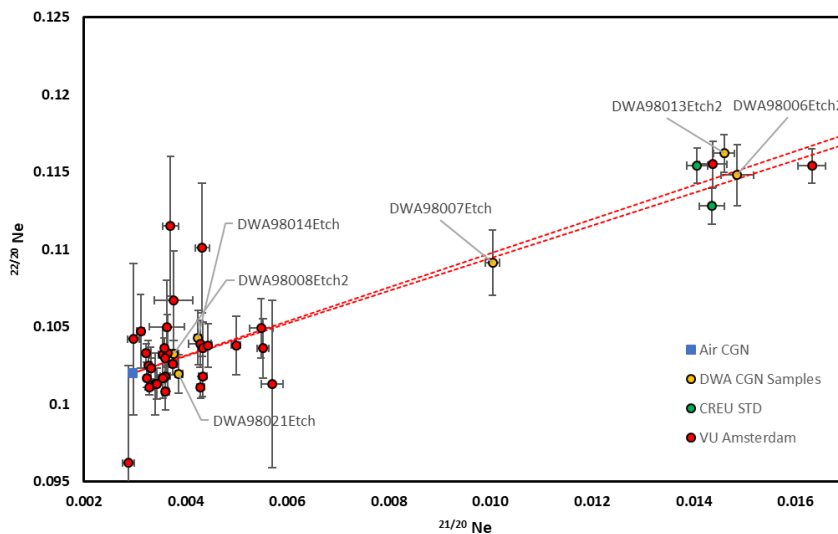
468

469 Fig. 4: (A) Microscope image of sample DWA98008-Silc8 after LA-ICP-MS analysis. Laser spots are
 470 visible, respective U-Pb Tera-Wasserburg plots are shown in (D-F). (B) Raman image of Silc8, area
 471 not visible on microscope image. Grey crosses indicate measured quartz spectra. White cross marked
 472 the occurrence of Calcite, which can be traced as a black line. Raman imaging shows multiple
 473 layering of silcrete filling the crack of the shattered quartz clast. Color variations are indicative of
 474 differences in crystal orientations (C) Respective Raman spectra for the quartz and calcite
 475 identification. (D-F) Tera-Wasserburg plots of Silc8 and respective U-Pb ages (red ellipses are
 476 considered outliers).

477 TCN Exposure Age Results

478 ^{21}Ne samples measured at the Noble Gas Laboratory in Cologne (Ritter et al., 2021) yield
 479 concentrations of $1.52 - 1.95 \times 10^7$ atoms/gr for shielded samples (DWA98008, 014, 021) and
 480 $6.30 - 9.60 \times 10^7$ atoms/gr for surface samples (DWA98006,007, 013). All samples are within 2
 481 sigma of the spallation line (Fig. 5). Compared to the ^{21}Ne concentrations of Van Der Wateren and
 482 Dunai (2001), the etched samples measured in Cologne reveal lower concentrations of up to 13%
 483 difference when comparing direct concentrations (average of five measured samples), however,
 484 within $\pm 1\sigma$ it reduces to $\sim 1.6\%$, agreeing within $\pm 2\sigma$ on average. We have excluded sample
 485 DWA98008, as it presumably contains a high abundance of non-cosmogenic Ne, as deduced from
 486 the significant concentration differences between the sample measured by Van Der Wateren and
 487 Dunai (2001) and the etched counterpart measured in Cologne (SI1_Supporting Information).
 488 Similar results and interpretations for sample DWA98008 were reported by Van Der Wateren and
 489 Dunai (2001).

490 Using the mean difference of $\sim 13\%$ between VU Amsterdam and Cologne Ne concentrations
 491 (SI1_Supporting Information), the data from Van Der Wateren and Dunai (2001) can be corrected
 492 for lab-specific differences. The corrected exposure ages are given in Table 3.



493

494 *Fig. 5: Triple isotope diagram indicating single-heat-step extraction of the Cologne laboratory*
 495 *(orange circles) compared to the multiple-heat-step extraction (red circles) of Van Der Wateren and*
 496 *Dunai (2001). Uncertainties are 1σ . The red stippled line indicates the Cologne laboratory spallation*
 497 *line (Ritter et al., 2021). Green circles indicate CREU1 measured during the analysis in Cologne.*

498 Calculated exposure ages derived from Cronus Earth (Balco et al., 2008) are summarised in
 499 Table 3. For the Kuiseb terrace, ^{21}Ne concentrations in shielded, pre-exposed samples
 500 (DWA98008, DWA98021), give a mean apparent age of 0.65 ± 0.04 Ma (external uncertainty $\pm 1\sigma$).
 501 The latter indicates that the non-cosmogenic component of DWA98008 has been removed by
 502 etching, indicating the identical apparent exposure age as DWA98021. Correction of the ^{21}Ne
 503 concentration of exposed rounded pebbles (DWA98007) from the top of the Carp Cliff terrace
 504 yields an exposure age of 3.2 ± 0.2 Ma ($\pm 1\sigma$ external uncertainty), being slightly older than
 505 calculated by Van Der Wateren and Dunai (2001), however, identical within the uncertainty.
 506 Exposed angular clasts (DWA98006) show a younger exposure age of 2.85 ± 0.19 Ma ($\pm 1\sigma$ external
 507 uncertainty). The latter is slightly older than in Van Der Wateren and Dunai (2001), which is
 508 identical within their uncertainty. A similar exposure age of 2.75 ± 0.18 Ma ($\pm 1\sigma$ external
 509 uncertainty) was derived from angular clasts from the Kamberg cliff (DWA98013) with. Angular
 510 clasts are assumed to be derived from local sources without significant pre-exposure from long
 511 transport times. Our results indicate that terrace abandonment and exposure to cosmic rays
 512 started at ~ 2.8 Ma (Fig. 6).

513 Table 3: TCN exposure ages.

	LSDn Exposure Age		
	Age [Ma]	Int. Unc. [Ma]	Ext. Unc. [Ma]
DWA98006Etch2	2.85	0.07	0.19
DWA98007Etch	3.85	0.07	0.25
Corr. DWA98007Etch2	3.20	0.05	0.20
DWA98008Etch2	0.66	0.02	0.05
DWA98021Etch	0.65	0.02	0.04
DWA98013Etch2	2.75	0.05	0.18
DWA98014Etch	0.90	0.02	0.06
DWA98001VU	5.35	0.23	0.41
DWA98002VU	3.98	0.32	0.40
DWA98003VU	1.08	0.13	0.15
DWA98005VU	0.58	0.06	0.07
DWA98019VU	0.49	0.05	0.06
DWA98024VU	1.27	0.12	0.14

7. Interpretation and Discussion

Our U-Pb ages are stratigraphically in the correct order, with the oldest U-Pb ages at the contact between quartz clast and filled rock fracture and the youngest age in the centre of the filled fracture (Table 2, Fig. 4). Recurrent U-Pb ages underpin and mark the main phase of silcrete, i.e. calcrete, formation. Groundwater calcrete formation, i.e., microscale silcrete formation, within the sediments of the proto-Kuiseb canyon (Karpfenkliff Conglomerate) took place between the Late Miocene (~7 Ma) and the Late Pliocene (~3 Ma, Fig. 6). The U-Pb silcrete ages suggest either persistent or alternating periods of wetter climate for groundwater calcrete formation.

Based on the causal relationship between silcrete and calcrete formation, our U-Pb silcrete ages indicate that environmental and climatic conditions during the Pliocene were sufficient to allow for carbonate leaching, transport and calcrete formation within the coarse-grained Karpfenkliff Conglomerate. However, whether the sampled groundwater calcrete is identical or synchronous with the prominent Kamberg Calcrete can be questioned, but we can narrow down the timing of major groundwater calcrete formation, previously assigned to the Late Miocene (Goudie et al., 2015; Ward, 1987) or Plio-Pleistocene (Pickford and Senut, 2000). Calcrete formation ceased during the Late Pliocene/Early Pleistocene by incision and groundwater lowering (Fig. 6).

Re-measured TCN ^{21}Ne surface exposure ages from amalgamated quartz clasts agree with the derived U-Pb silcrete chronology and are younger than the youngest U-Pb silcrete age obtained (Fig. 6), i.e., in stratigraphically correct order. The surface exposure ages mark the abandonment of the fluvial terraces and the onset of the Kuiseb River incision at ~2.8 Ma. The latter caused a groundwater lowering of the water table and the cessation of calcrete formation within the Karpfenkliff Conglomerate Formation. Re-measurements of the quartz clasts from the Oswater terrace downstream of the Karpfenkliff and Kamberg cliff sampling sites confirm the exposure ages previously obtained by Van Der Wateren and Dunai (2001). The exposure ages of the Karpfenkliff and Oswater terrace constrain the period of major canyon incision to ~2.8 -1.3 Ma (Fig. 6).

With the aid of absolute U-Pb silcrete and surface exposure dating, it is now possible to redefine depositional ages or depositional periods for sediments in the Central Namib Desert, some of which are widely used as marker horizons. Our U-Pb silcrete ages constrain the timing of sediment deposition within the Kuiseb Canyon (Karpfenkliff Conglomerate Formation) to be older than ~7 Ma, as silcrete formation within the conglomerates postdates deposition thereof (Fig. 6). The incision age of the Proto-Kuiseb and the subsequent deposition by the Karpfenkliff Conglomerate as proposed by Miller et al. (2021) of ~5 Ma, does not agree with our absolute U-Pb ages. If the relative biostratigraphic dating of Pickford and Senut (2000) is valid, the proto-Kuiseb canyon was filled by the Karpfenkliff Conglomerate Formation over a time period of up to 6-7 Ma

549 (Diamantornis corbetti at Elim ~14 15 Ma, see Pickford and Senut, 2000). Verification and
550 absolute direct dating of the Karpfenkliff Formation is still lacking and is a target for future studies.
551 Our fluvial chronology substantially supports the chronological data obtained by Van Der Wateren
552 and Dunai (2001).

553 **Pliocene Calcrete Formation – Steady State Climate**

554 Our U-Pb ages indicate a relatively calm or transitional phase between aggradation and backfilling
555 of the Proto-Kuiseb (and presumably other drainage systems such as the Swakop) and the
556 renewed incision by the recent Kuiseb River, throughout the Pliocene. U-Pb ages of microscale
557 silcrete from the same stratigraphic horizon indicate a long-term stable groundwater level, i.e. no
558 significant aggradation or degradation.

559 As the formation of groundwater calcrete is generally restricted to specific environmental
560 conditions, the existence and chronology of its formation in the Central Namib Desert now allows
561 us to relate these environmental conditions to specific episodes in the past and thus to obtain a
562 better and partly more quantitative paleoclimate and environmental reconstruction of the
563 Pliocene in the Central Namib Desert. We therefore interpret our U-Pb silcrete chronology as
564 marking the transition of the mean annual precipitation (MAP) from the upper potential limit of
565 approximately ~600 mm/yr or the lower potential limit of 50 mm/yr in the Kuiseb catchment
566 during the Late Miocene. Whether there was a climate change from, or a return to, wetter
567 conditions during the Pliocene cannot be determined from our U-Pb chronology. Calcrete
568 formation ceased with the incision of the Kuiseb River and a significant lowering of the
569 groundwater table.

570 Age information from the Kalahari Basin by Houben et al. (2020) indicated a shift towards more
571 arid conditions since ~12 Ma, which intensified at ~4 Ma (Houben et al., 2020; Miller et al., 2010).
572 Marine records off Namibia (Fig. 7, ODP 1081, Hoetzel et al., 2017) suggest a shift to more arid
573 conditions over the course of the Mid to Late Miocene, controlled by a gradual increase in the
574 upwelling activity of the Benguela Current, initiated by a strengthening of the meridional gradient.
575 This shift is supported by pollen data (Hoetzel et al., 2015; Dupont et al., 2013), indicating the
576 expansion of savanna grasslands (C4 expansion) in Namibia since ~8 Ma, with a subsequent shift
577 during the Pliocene to more shrubland and desert vegetation (Hoetzel et al., 2015).
578 Compound-specific hydrogen isotopes (ODP 1085, Dupont et al., 2013) indicate a change in the
579 precipitation source from the Atlantic to the Indian Ocean since ~8 Ma (Dupont et al., 2013).
580 Therefore, our U-Pb chronology of calcrete formation (~7-3 Ma) tracks the shift to more arid
581 conditions with a corresponding reduction in the MAP to allow calcrete formation. Nevertheless,
582 this transition and aridification of the Namib was slow, and regional SST records (ODP 1082,
583 Etourneau et al., 2009; ODP 1081, Rosell-Melé et al., 2014, Fig. 7), as well as global paleoclimate

584 records (benthic $\delta^{18}O$, Westerhold et al., 2020, Fig. 7) indicate a relatively stable climatic period.
585 Rosell-Melé et al. (2014) proposed, based on their marine SST record off Namibia (ODP 1082),
586 that the persistently warm Pliocene, with conditions analogue to a persistent Benguela 'El Niño',
587 ended at the transition to the Pleistocene (Fig. 6).

588 **Plio/Pleistocene Transition**

589 During the transition from the late Pliocene to the early Pleistocene, the Central Namib Desert
590 underwent large-scale landscape rejuvenation with drainage reorganisation and incision. This is
591 the same period, in which Miller et al. (2010) reconstructed the major desiccation of the Etosha
592 paleolake (Fig. 6). Based on U-Pb calcrete ages from the Kalahari basin, Houben et al. (2020)
593 proposed an intensification of arid conditions since ~ 3.8 Ma, older than our onset of more arid
594 conditions in the Central Namib at around 3 Ma. Higher offshore sedimentation rates off Namibia
595 may be associated with increased input of terrestrial material (Dupont et al., 2005) due to incision
596 of E-W flowing drainages into the Atlantic. The propagation of the Horingbaai fan-delta (between
597 Omaruru and the Ugab river) occurred approximately at the same time (2.7 -2.4 Ma) according to
598 Stollhofen et al. (2014), supporting the idea of large-scale landscape rejuvenation and incision of
599 multiple E-W flowing drainages in the Namib Desert.

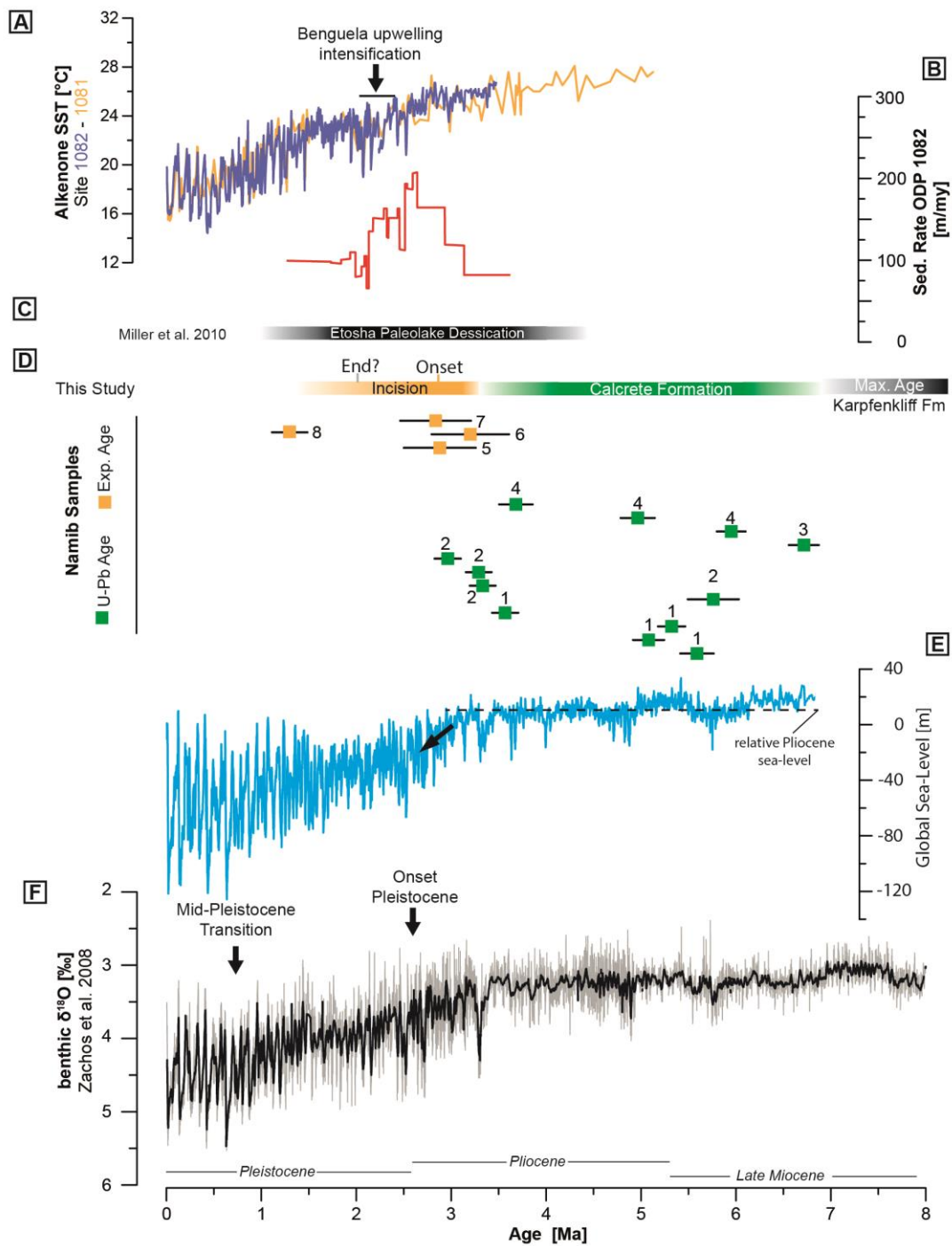
600 The underlying mechanism is still questionable, as several forcing factors could be responsible for
601 the incision of major E-W flowing river systems: climate change and variability, sea level change
602 and/or tectonic uplift. The latter was previously suggested by Ward (1987) and attributed to a
603 late Neogene epeirogenic uplift. Stollhofen et al. (2014) also suggest that uplift could be one of the
604 causes and/or at least a contributor to other factors, such as climate.

605 Data from the marine realm off Namibia suggest a further step towards more extreme arid
606 conditions during the Plio-/Pleistocene transition (Fig. 6). Local SST records (ODP 1082,
607 Etourneau et al., 2009; ODP 1081, Rosell-Melé et al., 2014, Fig. 7) indicate the onset of decreasing
608 SSTs at ~ 2.7 -2.5 Ma and the significant shift towards increased upwelling activity of colder water
609 masses in the Benguela Current since ~ 2.2 Ma (Dupont et al., 2005; Marlow et al., 2000; Etourneau
610 et al., 2009). The significant decrease in SSTs correlates with the further intensification of
611 Northern Hemisphere glaciation since ~ 2.7 Ma (Ruggieri et al., 2009). The pollen record (ODP
612 1082) of (Dupont, 2006) shows that arid to semi-arid biomes were rather limited prior to ~ 2.7
613 Ma, and that their concentration increases with higher variability since then, reflecting the
614 intensification of arid conditions in the Central Namib Desert (Dupont, 2006).

615 Vegetation change may be a major cause of the exposure of landscapes to accelerated erosion.
616 Major river incision in the Central Namib Desert thus occurred during a period of climate change
617 and greater climate variability compared to the more persistently stable Pliocene (Rosell-Melé et

618 al., 2014), with the intensification of arid conditions in southern Africa, synchronous with major
619 global changes. We therefore propose that the major river incision of the Kuseb River at the
620 Plio-/Pleistocene transition was caused by a shift to more arid conditions with decreasing
621 precipitation, resulting in reduced river discharge, river steepening and incision (e.g. Whipple and
622 Tucker, 1999; Bonnet and Crave, 2003; Molnar, 2001; Cooper et al., 2016). Catchment and river
623 systems such as the Kuseb (and/or river systems such as the Swakop), which had reached a
624 steady-state during the more stable Pliocene, had to adapt to the new boundary conditions, which
625 is in line with the global increase in erosion rates at the Plio-/Pleistocene transition (Herman et
626 al., 2013; Herman and Champagnac, 2016). A major vegetation shift towards more arid biomes
627 and sparser vegetation cover increased the susceptibility of landscapes to erosion. The global
628 sea-level drop at the Plio-/Pleistocene transition may have had an additional impact on drainage
629 base levels.

630 The incision of the recent Kuseb River can be constrained to a period between the derived terrace
631 ages of ~2.8 and ~1.3 Ma (minimum age of the Oswater bedrock river terrace). The actual period
632 of incision may be even shorter, given the cessation of fluvial sediment deposition offshore at
633 ~2 Ma (Dupont et al., 2005). Deposition of the Oswater Formation indicates a phase of
634 aggradation sometime after ~1.3 Ma, followed by an incision into the recent bed of the Kuseb
635 River.



636

637 Fig. 6: Compilation of paleoclimate records. (A) Alkenone SSTs from ODP 1082 (Etourneau et al.,
 638 2009) and ODP 1081 (Rosell-Melé et al., 2014). Intensification of Benguela upwelling according to
 639 Etourneau et al. (2009). (B) Sedimentation rate of ODP 1082 for the Plio/Pleistocene transition
 640 (Dupont, 2006). (C) Desiccation of the Etosha paleolake from Miller et al. (2010). (D) U-Pb silcrete
 641 and surface exposure ages (this study). Numbers indicate identical clasts. 1 - DWA98008-Silc3, 2 -
 642 DWA98008-Silc4, 3 - DWA98008-Silc7, 4 - DWA98008-Silc8, 5 - DWA98013, 6 - DWA98007, 7-
 643 DWA98006, 8 - DWA98024. (E) Global Sea-Level curve from Hansen et al. (2013). Black dashed line
 644 indicates relative mean sea-level during the Pliocene, followed by the global decrease since the Plio-
 645 /Pleistocene transition. (F) Global Cenozoic reference benthic foraminifer oxygen isotope dataset
 646 (CENOGRID) from Westerhold et al. (2020).

647 **Conclusion**

648 Our study demonstrates that microscale silcrete from the Central Namib Desert can be dated using
649 U-Pb LA-ICP-MS, and that layered silcrete incrustations can be used as paleoclimate archives.
650 LA-ICP-MS U-Pb dating of silcrete has advantages over bulk carbonate analysis because it is less
651 affected by potential interferences and contamination. The combined dating approach with
652 additional ^{21}Ne exposure age dating allows us to reconstruct major paleoclimate and landscape
653 changes since the Late Miocene for the Central Namib Desert. We can corroborate previously
654 obtained chronological data from Van Der Wateren and Dunai (2001) and place absolute age
655 constraints on some sediments from the Central Namib Desert, some of which are used as marker
656 horizons throughout the region. Our chronology of groundwater calcrete formation and river
657 incision adds crucial information with absolute dates to the 'Namib Group'. Although specific
658 precipitation ranges for calcrete formation are still being debated, we can assign potential
659 precipitation ranges and their shifts to specific time episodes and thus provide a semi-quantitative
660 picture of the aridification of the Central Namib Desert during the Late Miocene to the
661 Plio-/Pleistocene. Our terrestrial paleoclimate record of microscale silcrete formation, i.e.,
662 calcrete formation, supports the marine evidence for a persistently stable Pliocene climate in the
663 Central Namib Desert. The cessation of groundwater calcrete formation was caused by the deep
664 incision of the Kuiseb River (presumably synchronous with other E-W flowing drainage systems
665 of the Central Namib Desert) at the Plio-/Pleistocene transition, which can be explained by the
666 intensification of aridity, vegetation change, and presumably global sea-level drop. Global climate
667 change with the onset of the Pleistocene was most likely the major forcing factor for major
668 landscape rejuvenation and change in the Central Namib Desert. Precipitation decline in the
669 Kuiseb River catchment is identified as the tipping point for the local climate and landscape
670 response.

671 **Acknowledgements:**

672 We want to thank our colleagues from the Gobabeb Research Station for their help during
673 fieldwork in 2018. Moreover, we want to thank our preparation workshops for preparation of thin
674 sections and pucks. We also want to thank Prof. A. Woodland, for his support with Raman
675 spectroscopy. This project is affiliated with the Collaborative Research Center (CRC) 1211, funded
676 by the German Science Foundation (DFG), Projektnummer 268236062. This is FIERCE
677 contribution number XXX.

678 **Author Contribution:**

679 B.R. fieldwork, sample preparation, ^{21}Ne noble gas analytic, data evaluation, manuscript writing.
680 R.A. U-Pb dating, sample analysis thin section, Raman, data analysis, manuscript writing. A.R.

681 Raman, F.M.v.d.W. fieldwork, T.J.D. fieldwork, data evaluation. A.G. data analysis. All authors
682 reviewed the manuscript.

683 **Additional Information**

684 **Declaration of interest:** The authors declare that the research was conducted in the absence of
685 any commercial or financial relationships that could be construed as a potential conflict of
686 interest.

687 **Data availability statement:** All data generated or analysed during this study are included in this
688 published article (and its supporting information files).

689 **References**

690

691 Alonso-Zarza, A. M.: Palaeoenvironmental significance of palustrine carbonates and calcretes in
692 the geological record, *Earth-Science Reviews*, 60, 261-298, 2003.
693

694 Alonso-Zarza, A. M. and Wright, V.: Calcretes, *Developments in Sedimentology*, 61, 225-267, 2010.
695

696 Balco, G., Stone, J. O., Lifton, N. A., and Dunai, T. J.: A complete and easily accessible means of
697 calculating surface exposure ages or erosion rates from $(10)\text{Be}$ and $(26)\text{Al}$ measurements,
698 *Quaternary Geochronology*, 3, 174-195, 10.1016/j.quageo.2007.12.001, 2008.
699

700 Bierman, P. R. and Caffee, M.: Slow rates of rock surface erosion and sediment production across
701 the Namib Desert and escarpment, southern Africa, *Am. J. Sci.*, 301, 326-358, 2001.
702

703 Bonnet, S. and Crave, A.: Landscape response to climate change: Insights from experimental
704 modeling and implications for tectonic versus climatic uplift of topography, *Geology*, 31, 123-126,
705 2003.
706

707 Branca, M., Masi, U., and Voltaggio, M.: An unsuccessful attempt at U/Th dating of soil calcretes
708 from the Doukkali area (western Morocco) and environmental implications, *Geochemistry*, 65,
709 347-356, 2005.
710

711 Butt, C., Horwitz, R., and Mann, A.: Uranium occurrences in calcrete and associated sediments in
712 Western Australia, Commonwealth Scientific and Industrial Research Organization, 1977.
713

714 Candy, I. and Black, S.: The timing of Quaternary calcrete development in semi-arid southeast
715 Spain: investigating the role of climate on calcrete genesis, *Sedimentary Geology*, 218, 6-15, 2009.
716

717 Candy, I., Black, S., and Sellwood, B. W.: Quantifying time scales of pedogenic calcrete formation
718 using U-series disequilibria, *Sedimentary Geology*, 170, 177-187, 10.1016/j.sedgeo.2004.07.003,
719 2004.
720

721 Cooper, F. J., Adams, B., Blundy, J., Farley, K., McKeon, R., and Ruggiero, A.: Aridity-induced Miocene
722 canyon incision in the Central Andes, *Geology*, 44, 675-678, 2016.
723

724 Dupont, L. M.: Late Pliocene vegetation and climate in Namibia (southern Africa) derived from
725 palynology of ODP site 1082, *Geochemistry Geophysics Geosystems*, 7, Q05007,
726 doi:10.1029/102005GC001208, 2006.
727

728 Dupont, L. M., Rommerskirchen, F., Mollenhauer, G., and Schefuß, E.: Miocene to Pliocene changes
729 in South African hydrology and vegetation in relation to the expansion of C4 plants, *Earth and
730 Planetary Science Letters*, 375, 408-417, 2013.
731

732 Dupont, L. M., Donner, B., Vidal, L., Pérez, E. M., and Wefer, G.: Linking desert evolution and coastal
733 upwelling: Pliocene climate change in Namibia, *Geology*, 33, 461-464, 2005.
734

735 Etourneau, J., Martinez, P., Blanz, T., and Schneider, R.: Pliocene–Pleistocene variability of
736 upwelling activity, productivity, and nutrient cycling in the Benguela region, *Geology*, 37, 871-874,
737 2009.
738

739 Geological Survey of Namibia: Geological Map 2314 Kuiseb 1:250 000 ESRI Shapefile, Geological
740 Survey of Namibia, Windhoek, Geological Series, 2016.
741

742 Gerdes, A. and Zeh, A.: Combined U–Pb and Hf isotope LA–(MC–) ICP–MS analyses of detrital
743 zircons: comparison with SHRIMP and new constraints for the provenance and age of an
744 Armorican metasediment in Central Germany, *Earth and Planetary Science Letters*, 249, 47-61,
745 2006.
746

747 Gerdes, A. and Zeh, A.: Zircon formation versus zircon alteration—new insights from combined U–
748 Pb and Lu–Hf in-situ LA–ICP–MS analyses, and consequences for the interpretation of Archean
749 zircon from the Central Zone of the Limpopo Belt, *Chemical Geology*, 261, 230-243, 2009.
750

751 Geyh, M. A. and Eitel, B.: Radiometric dating of young and old calcrete, *Radiocarbon*, 40, 795-802,
752 1997.
753

754 Goudie, A.: Duricrusts in tropical and subtropical landscapes, *Duricrusts in Tropical and
755 Subtropical Landscapes*, 1973.
756

757 Goudie, A.: Calcrete, *Chemical Sediments and Geomorphology: precipitates and residua in the
758 near-surface environment*, 1983.
759

760 Goudie, A.: Organic agency in calcrete development, *Journal of Arid Environments*, 32, 103-110,
761 1996.
762

763 Goudie, A.: Duricrusts and landforms, in: *Geomorphology and soils*, Routledge, 37-57, 2020.
764

765 Goudie, A. and Viles, H.: *Landscapes and landforms of Namibia*, Springer 2014.
766

- 767 Goudie, A., Viles, H., Goudie, A., and Viles, H.: Calcretes: The Kamberg Calcrete Formation and the
768 Karpencliff Conglomerate, Landscapes and Landforms of Namibia, 111-114, 2015.
769
- 770 Hansen, J., Sato, M., Russell, G., and Kharecha, P.: Climate sensitivity, sea level and atmospheric
771 carbon dioxide, *Philosophical Transactions of the Royal Society A: Mathematical, Physical and*
772 *Engineering Sciences*, 371, 20120294, 2013.
773
- 774 Herman, F. and Champagnac, J. D.: Plio-Pleistocene increase of erosion rates in mountain belts in
775 response to climate change, *Terra Nova*, 28, 2-10, 2016.
776
- 777 Herman, F., Seward, D., Valla, P. G., Carter, A., Kohn, B., Willett, S. D., and Ehlers, T. A.: Worldwide
778 acceleration of mountain erosion under a cooling climate, *Nature*, 504, 423-426, 2013.
779
- 780 Hoetzel, S., Dupont, L. M., and Wefer, G.: Miocene–Pliocene vegetation change in south-western
781 Africa (ODP Site 1081, offshore Namibia), *Palaeogeography, Palaeoclimatology, Palaeoecology*,
782 423, 102-108, 2015.
783
- 784 Hoetzel, S., Dupont, L. M., Marret, F., Jung, G., and Wefer, G.: Steps in the intensification of Benguela
785 upwelling over the Walvis Ridge during Miocene and Pliocene, *International Journal of Earth*
786 *Sciences*, 106, 171-183, 2017.
787
- 788 Horstwood, M. S., Košler, J., Gehrels, G., Jackson, S. E., McLean, N. M., Paton, C., Pearson, N. J.,
789 Sircombe, K., Sylvester, P., and Vermeesch, P.: Community-derived standards for LA-ICP-MS U-
790 (Th-) Pb geochronology–Uncertainty propagation, age interpretation and data reporting,
791 *Geostandards and Geoanalytical Research*, 40, 311-332, 2016.
792
- 793 Houben, G. J., Kaufhold, S., Miller, R. M., Lohe, C., Hinderer, M., Noll, M., Hornung, J., Joseph, R.,
794 Gerdes, A., and Sitnikova, M.: Stacked megafans of the Kalahari Basin as archives of
795 paleogeography, river capture, and Cenozoic paleoclimate of southwestern Africa, *Journal of*
796 *Sedimentary Research*, 90, 980-1010, 2020.
797
- 798 Jacobson, P. J., Jacobson, K. M., and Seely, M. K.: Ephemeral rivers and their catchments: Sustaining
799 people and development in Namibia, *Desert Research Foundation of Namibia, Windhoek*, 160
800 pp.1995.
801
- 802 Kelly, M., Black, S., and Rowan, J.: A calcrete-based U/Th chronology for landform evolution in the
803 Sorbas basin, southeast Spain, *Quaternary Science Reviews*, 19, 995-1010, 2000.
804
- 805 King, L.: The geomorphology of the Eastern and Southern districts of Southern Rhodesia, *South*
806 *African Journal of Geology*, 54, 33-64, 1951.
807
- 808 King, L. C.: Pediplanation and isostasy: an example from South Africa, *Quarterly Journal of the*
809 *Geological Society*, 111, 353-359, 1955.
810
- 811 Korn, H. and Martin, H.: The Pleistocene in South West Africa, *Proceedings of the 3rd Pan-African*
812 *Congress on Prehistory*, 14-22,
813

814 Lancaster, N.: Paleoenvironments in the Tsondab valley, Central Namib desert, in: Palaeoecology
815 of Africa and of the Surrounding Islands and Antarctica, edited by: Coetzee, J. A., and van Zinderen
816 Bakker, E. M., Balkema, Cape Town, 411-419, 1984.
817

818 Lifton, N., Sato, T., and Dunai, T. J.: Scaling in situ cosmogenic nuclide production rates using
819 analytical approximations to atmospheric cosmic-ray fluxes, *Earth and Planetary Science Letters*,
820 386, 149-160, 10.1016/j.epsl.2013.10.052, 2014.
821

822 Ludwig, K. R.: User's manual for Isoplot 3.75., Berkeley Geochronological Center Special
823 Publication No. 5., 2012.
824

825 Mack, G. H. and James, W.: Paleoclimate and the global distribution of paleosols, *The Journal of*
826 *Geology*, 102, 360-366, 1994.
827

828 Maher, K., Wooden, J., Paces, J., and Miller, D.: ²³⁰Th-U dating of surficial deposits using the ion
829 microprobe (SHRIMP-RG): A microstratigraphic perspective, *Quaternary International*, 166, 15-
830 28, 2007.
831

832 Mann, A. and Horwitz, R.: Groundwater calcrete deposits in Australia some observations from
833 Western Australia, *Journal of the Geological Society of Australia*, 26, 293-303, 1979.
834

835 Marlow, J. R., Lange, C. B., Wefer, G., and Rosell-Melé, A.: Upwelling intensification as part of the
836 Pliocene-Pleistocene climate transition, *Science*, 290, 2288-2291, 2000.
837

838 McBride, E. F.: Quartz cement in sandstones: a review, *Earth-Science Reviews*, 26, 69-112, 1989.
839

840 Miller, R.: The Geology of Namibia, Ministry of Mines and Energy - Geological Survey Namibia, 3,
841 25-21, 2008.
842

843 Miller, R. M., Pickford, M., and Senut, B.: The geology, palaeontology and evolution of the Etosha
844 Pan, Namibia: Implications for terminal Kalahari deposition, *South African Journal of Geology*,
845 113, 307-334, 2010.
846

847 Miller, R. M., Krapf, C., Hoey, T., Fitchett, J., Nguno, A.-K., Muyambas, R., Ndeutepo, A., Medialdea,
848 A., Whitehead, A., and Stengel, I.: A sedimentological record of fluvial-aeolian interactions and
849 climate variability in the hyperarid northern Namib Desert, Namibia, *South African Journal of*
850 *Geology*, 124, 575-610, 2021.
851

852 Milnes, A. and Thiry, M.: Silcretes, in: *Developments in earth surface processes*, Elsevier, 349-377,
853 1992.
854

855 Milnes, A., Wright, M., and Thiry, M.: Silica accumulations in saprolites and soils in South Australia,
856 Occurrence, characteristics, and genesis of carbonate, gypsum, and silica accumulations in soils,
857 26, 121-149, 1991.
858

- 859 Molnar, P.: Climate change, flooding in arid environments, and erosion rates, *Geology*, 29, 1071-
860 1074, 2001.
861
- 862 Nash, D. J. and Shaw, P. A.: Silica and carbonate relationships in silcrete-calcrete intergrade
863 duricrusts from the Kalahari of Botswana and Namibia, *Journal of African Earth Sciences*, 27, 11-
864 25, 1998.
865
- 866 Nash, D. J. and Smith, R. F.: Multiple calcrete profiles in the Tabernas Basin, southeast Spain: their
867 origins and geomorphic implications, *Earth Surface Processes and Landforms: The Journal of the*
868 *British Geomorphological Group*, 23, 1009-1029, 1998.
869
- 870 Netterberg, F.: The interpretation of some basic calcrete types, *The South African Archaeological*
871 *Bulletin*, 24, 117-122, 1969.
872
- 873 Neymark, L.: Potential effects of alpha-recoil on uranium-series dating of calcrete, *Chemical*
874 *Geology*, 282, 98-112, 2011.
875
- 876 Neymark, L.: Uranium-Lead dating, opal, 2014.
877
- 878 Ollier, C.: Outline geological and geomorphic history of the central Namib Desert, Madoqua, 1977,
879 207-212, 1977.
880
- 881 Oster, J. L., Kitajima, K., Valley, J. W., Rogers, B., and Maher, K.: An evaluation of paired $\delta^{18}O$ and
882 $(^{234}U/^{238}U)$ 0 in opal as a tool for paleoclimate reconstruction in semi-arid environments,
883 *Chemical Geology*, 449, 236-252, 2017.
884
- 885 Partridge, T. and Maud, R.: Geomorphic evolution of southern Africa since the Mesozoic, *South*
886 *African Journal of Geology*, 90, 179-208, 1987.
887
- 888 Pickford, M. and Senut, B.: Geology and Palaeobiology of the Central and Southern Namib Desert,
889 Southwestern Africa: Geology and History of Study, Geological Survey 2000.
890
- 891 Pickford, M., Senut, B., and Dauphin, Y.: Biostratigraphy of the Tsondab sandstone (Namibia) based
892 on gigantic avian eggshells, *Geobios*, 28, 85-98, 1995.
893
- 894 Pickford, M., Senut, B., Gommery, D., Andrews, P., and Banham, P.: Sexual dimorphism in
895 *Morotopithecus bishopi*, an early Middle Miocene hominoid from Uganda, Late Cenozoic
896 environments and hominid evolution: a tribute to Bill Bishop, 27-38, 1999.
897
- 898 Rasbury, E. T. and Cole, J. M.: Directly dating geologic events: U-Pb dating of carbonates, *Reviews*
899 *of Geophysics*, 47, 2009.
900
- 901 Repka, J. L., Anderson, R. S., and Finkel, R. C.: Cosmogenic dating of fluvial terraces, Fremont River,
902 Utah, *Earth and Planetary Science Letters*, 152, 59-73, [http://dx.doi.org/10.1016/S0012-
903 821X\(97\)00149-0](http://dx.doi.org/10.1016/S0012-821X(97)00149-0), 1997.
904

- 905 Retallack, G. J.: The environmental factor approach to the interpretation of paleosols, *Factors of*
906 *soil formation: A fiftieth anniversary retrospective*, 33, 31-64, 1994.
907
- 908 Richards, K. and Richards, K.: *River channels: environment and process*, Basil Blackwell 1987.
909
- 910 Ritter, B., Vogt, A., and Dunai, T. J.: Technical Note: Noble gas extraction procedure and
911 performance of the Cologne Helix MC Plus multi-collector noble gas mass spectrometer for
912 cosmogenic neon isotope analysis, *Geochronology*, 2021, 2021.
913
- 914 Rosell-Melé, A., Martínez-García, A., and McClymont, E. L.: Persistent warmth across the Benguela
915 upwelling system during the Pliocene epoch, *Earth and Planetary Science Letters*, 386, 10-20,
916 2014.
917
- 918 Ruggieri, E., Herbert, T., Lawrence, K. T., and Lawrence, C. E.: Change point method for detecting
919 regime shifts in paleoclimatic time series: application to $\delta^{18}O$ time series of the Plio-Pleistocene,
920 *Paleoceanography*, 24, 2009.
921
- 922 Rutter, E.: Pressure solution in nature, theory and experiment, *Journal of the Geological Society*,
923 140, 725-740, 1983.
924
- 925 Scardia, G., Parenti, F., Miggins, D. P., Gerdes, A., Araujo, A. G., and Neves, W. A.: Chronologic
926 constraints on hominin dispersal outside Africa since 2.48 Ma from the Zarqa Valley, Jordan,
927 *Quaternary Science Reviews*, 219, 1-19, 2019.
928
- 929 Senut, B.: Fossil ratite eggshells: a useful tool for Cainozoic biostratigraphy in Namibia,
930 *Communications of the geological Survey of Namibia*, 12, 367-373, 2000.
931
- 932 Sorby, H. C.: II. The Bakerian lecture.—On the direct correlation of mechanical and chemical forces,
933 *Proceedings of the Royal Society of London*, 538-550, 1863.
934
- 935 Stacey, J. t. and Kramers, J.: Approximation of terrestrial lead isotope evolution by a two-stage
936 model, *Earth and planetary science letters*, 26, 207-221, 1975.
937
- 938 Stokes, M., Nash, D. J., and Harvey, A. M.: Calcrete 'fossilisation' of alluvial fans in SE Spain: The roles
939 of groundwater, pedogenic processes and fan dynamics in calcrete development, *Geomorphology*,
940 85, 63-84, 2007.
941
- 942 Stollhofen, H., Stanistreet, I. G., von Hagke, C., and Nguno, A.: Pliocene–Pleistocene climate change,
943 sea level and uplift history recorded by the Horingbaai fan-delta, NW Namibia, *Sedimentary*
944 *geology*, 309, 15-32, 2014.
945
- 946 Stone, A.: Age and dynamics of the Namib Sand Sea: A review of chronological evidence and
947 possible landscape development models, *Journal of African Earth Sciences*, 82, 70-87, 2013.
948
- 949 Summerfield, M.: Silcrete as a palaeoclimatic indicator: evidence from southern Africa,
950 *Palaeogeography, Palaeoclimatology, Palaeoecology*, 41, 65-79, 1983a.

951

952 Summerfield, M. A.: Petrography and diagenesis of silcrete from the Kalahari Basin and Cape
 953 coastal zone, Southern Africa, *Journal of Sedimentary Research*, 53, 895-909, 1983b.
 954

955 Taylor, G. and Eggleton, R.: Silcrete: an Australian perspective, *Australian Journal of Earth
 956 Sciences*, 64, 987-1016, 2017.
 957

958 Tera, F. and Wasserburg, G.: U-Th-Pb systematics in lunar highland samples from the Luna 20 and
 959 Apollo 16 missions, *Earth and Planetary Science Letters*, 17, 36-51, 1972.
 960

961 Van der Wateren, F. M. and Dunai, T. J.: Late Neogene passive margin denudation history -
 962 cosmogenic isotope measurements from the central Namib desert, *Global and Planetary Change*,
 963 30, 271-307, 10.1016/s0921-8181(01)00104-7, 2001.
 964

965 Vermeesch, P., Fenton, C., Kober, F., Wiggs, G., Bristow, C. S., and Xu, S.: Sand residence times of one
 966 million years in the Namib Sand Sea from cosmogenic nuclides, *Nature Geoscience*, 3, 862-865,
 967 2010.
 968

969 Vermeesch, P., Balco, G., Blard, P. H., Dunai, T. J., Kober, F., Niedermann, S., Shuster, D. L., Strasky,
 970 S., Stuart, F. M., Wieler, R., and Zimmermann, L.: Interlaboratory comparison of cosmogenic Ne-21
 971 in quartz, *Quaternary Geochronology*, 26, 20-28, doi.org/10.1016/j.quageo.2012.11.009, 2015.
 972

973 Ward, J. and Corbett, I.: Towards an age for the Namib, *Namib ecology*, 25, 17-26, 1990.
 974

975 Ward, J. D.: The Cenozoic succession in the Kuiseb valley, central Namib desert, *Geological Survey
 976 of Namibia Memoir*, Windhoek 1987.
 977

978 Ward, J. D., Seely, M. K., and Lancaster, N.: On the antiquity of the Namib, *South African Journal of
 979 Science*, 79, 175-183, 1983.
 980

981 Weissel, J. K. and Seidl, M. A.: Inland propagation of erosional escarpments and river profile
 982 evolution across the southeast Australian passive continental margin, *Geophysical Monograph-
 983 American Geophysical Union*, 107, 189-206, 1998.
 984

985 Wendt, I. and Carl, C.: U/Pb dating of discordant 0.1 Ma old secondary U minerals, *Earth and
 986 Planetary Science Letters*, 73, 278-284, 1985.
 987

988 Westerhold, T., Marwan, N., Drury, A. J., Liebrand, D., Agnini, C., Anagnostou, E., Barnet, J. S., Bohaty,
 989 S. M., De Vleeschouwer, D., and Florindo, F.: An astronomically dated record of Earth's climate and
 990 its predictability over the last 66 million years, *Science*, 369, 1383-1387, 2020.
 991

992 Whipple, K. X. and Tucker, G. E.: Dynamics of the stream-power river incision model: Implications
 993 for height limits of mountain ranges, landscape response timescales, and research needs, *Journal
 994 of Geophysical Research: Solid Earth*, 104, 17661-17674, 1999.
 995

- 996 Wilson, M. J.: Dissolution and formation of quartz in soil environments: A review, *Soil Sci. Annu*,
997 71, 3-14, 2020.
998
- 999 Yaalon, D. H. and Ward, J. D.: Observations on calcrete and recent calcic horizons in relation to
1000 landforms, central Namib desert, in: *Palaeoecology of Africa and of the Surrounding Islands and*
1001 *Antarctica*, edited by: Coetzee, J. A., and van Zinderen Bakker, E. M., Balkema, Cape Town, 183-186,
1002 1982.
- 1003 Candy, I., Black, S., 2009. The timing of Quaternary calcrete development in semi-arid southeast
1004 Spain: Investigating the role of climate on calcrete genesis. *Sedimentary Geology* 218, 6–15.
1005 <https://doi.org/10.1016/j.sedgeo.2009.03.005>
- 1006 Maher, K., Wooden, J.L., Paces, J.B., Miller, D.M., 2007. ^{230}Th -U dating of surficial deposits using
1007 the ion microprobe (SHRIMP-RG): A microstratigraphic perspective. *Quaternary International*,
1008 *Dating Quaternary sediments and landforms in Drylands* 166, 15–28.
1009 <https://doi.org/10.1016/j.quaint.2007.01.003>
- 1010 Neymark, L., 2015. Uranium–Lead Dating, Opal. [https://doi.org/10.1007/978-94-007-6326-](https://doi.org/10.1007/978-94-007-6326-5_263-1)
1011 [5_263-1](https://doi.org/10.1007/978-94-007-6326-5_263-1)
- 1012 Neymark, L.A., 2011. Potential effects of alpha-recoil on uranium-series dating of calcrete.
1013 *Chemical Geology* 282, 98–112. <https://doi.org/10.1016/j.chemgeo.2011.01.013>
- 1014 Neymark, L.A., Amelin, Y., Paces, J.B., Peterman, Z.E., 2002. U-Pb ages of secondary silica at Yucca
1015 Mountain, Nevada: implications for the paleohydrology of the unsaturated zone. *Applied*
1016 *Geochemistry* 17, 709–734. [https://doi.org/10.1016/S0883-2927\(02\)00032-X](https://doi.org/10.1016/S0883-2927(02)00032-X)
- 1017 Neymark, L.A., Amelin, Y.V., Paces, J.B., 2000. ^{206}Pb – ^{230}Th – ^{234}U – ^{238}U and ^{207}Pb – ^{235}U
1018 geochronology of Quaternary opal, Yucca Mountain, Nevada. *Geochimica et Cosmochimica Acta*
1019 64, 2913–2928. [https://doi.org/10.1016/S0016-7037\(00\)00408-7](https://doi.org/10.1016/S0016-7037(00)00408-7)
- 1020 Oster, J.L., Kitajima, K., Valley, J.W., Rogers, B., Maher, K., 2017. An evaluation of paired $\delta^{18}\text{O}$ and
1021 $(^{234}\text{U}/^{238}\text{U})_0$ in opal as a tool for paleoclimate reconstruction in semi-arid environments.
1022 *Chemical Geology* 449, 236–252. <https://doi.org/10.1016/j.chemgeo.2016.12.009>
- 1023 Scardia, G., Parenti, F., Miggins, D.P., Gerdes, A., Araujo, A.G.M., Neves, W.A., 2019. Chronologic
1024 constraints on hominin dispersal outside Africa since 2.48 Ma from the Zarqa Valley, Jordan.
1025 *Quaternary Science Reviews* 219, 1–19. <https://doi.org/10.1016/j.quascirev.2019.06.007>
- 1026